One-dimensional Variational Retrieval of Temperature and Humidity Profiles from the FY4A GIIRS

Qiumeng XUE[1], Li GUAN* [1], and Xiaoning SHI[2]

[1] *Collaborative Innovation Center on Forecast and Evaluation of Meteorological Disasters, Key Laboratory for Aerosol-Cloud-Precipitation of China Meteorological Administration, Nanjing University of Information Science and Technology, Nanjing, Jiangsu 210044, China.*

[2] *Department of Mathematics, University of Wisconsin-Madison, Madison, Wisconsin, 53706, USA*

ABSTRACT

A physical retrieval approach based on the one-dimensional variational (1D-Var) algorithm is applied in this paper to simultaneously retrieve atmospheric temperature and humidity profiles under both clear-sky and partly cloudy conditions from FY-4A GIIRS (geostationary interferometric infrared sounder) observations. Radiosonde observations from upper-air stations in China and level 2 operational products from the Chinese National Satellite Meteorological Center (NSMC) during the periods from December 2019 to January 2020 (winter) and from July 2020 to August 2020 (summer) are used to validate the accuracies of the retrieved temperature and humidity profiles. Comparing the 1D-Var-retrieved profiles to radiosonde data, the accuracy of the temperature retrievals at each vertical level of the troposphere is characterized by a root mean square error (RMSE) within 2 K except for at the bottom level of the atmosphere under clear conditions. The RMSE slightly increases in the higher atmospheric layers, owing to the

*Corresponding author : Li GUAN
Email: liguan@nuist.edu.cn

lack of temperature sounding channels. Under partly cloudy conditions, the temperature at each vertical level can be obtained, while the level-2 operational products obtain values only at altitudes above the cloud top. In addition, the accuracy of the retrieved temperature profiles is greatly improved compared with the accuracies of the operational products. With respect to the humidity retrievals, the mean RMSEs in the troposphere in winter and summer are both within 2 g/kg. Moreover, the retrievals performed better compared with the ERA5 reanalysis data between 800 hPa and 300 hPa both in summer and winter in the RMSE sense.

Key words: temperature and humidity profiles; one-dimensional variational (1D-Var); GIIRS; hyperspectral data

https://doi.org/10.1007/s00376-021-1032-z

Article Highlights:

- The 1D-Var physical retrieval algorithm is utilized to retrieve the atmospheric profiles under both clear-sky and partly cloudy conditions.
- The 1D-Var-retrieved atmospheric profiles can be produced at each vertical level while the NSMC level-2 operational products obtain temperature values only at altitudes above the cloud top and no humidity retrievals.
- The accuracy of the 1D-Var-retrieved temperature profiles is greatly improved compared with the accuracies of the NSMC operational level-2 products.

1. Introduction

Atmospheric temperature and humidity profiles are essential to climate research. Continuous and frequent atmospheric temperature and humidity profiles are of great significance for improving the accuracy of nowcasting applications and situation awareness. Atmospheric temperature and humidity profiles from conventional radiosonde data have high representativeness and dependability. However, due to their low temporal and spatial resolutions, it is difficult for radiosonde measurements to meet the requirements of the development of global climate and weather models. To solve this problem, satellite-based hyperspectral infrared (IR) sounders have been developed in recent decades due to their unique advantages (Menzel et al., 2018). Hyperspectral infrared sounders onboard meteorological satellites can monitor vertical temperature and humidity structures on a global scale with a high temporal resolution (Yang et al., 2017). In addition, hyperspectral infrared sounders have thousands of channels with high vertical resolution, which can display a more detailed and accurate atmospheric temperature and humidity vertical structure (Strow et al., 2003; Pougatchev et al., 2009).

Temperature and humidity profiles can be obtained from hyperspectral infrared sounder measurements by combining the IR radiation transmission model with a retrieval algorithm. Much work so far has focused on these retrieval algorithms. In 1956, King first proposed the concept of using radiation received by infrared sounders to retrieve atmospheric temperature (King, 1956). Kaplan reported that atmospheric temperatures at different heights can be retrieved by using radiation from different spectral regions originating from different atmospheric layers (Kaplan, 1956). Currently, the main retrieval methods can generally be divided into three types: statistical approaches, machine learning approaches, and physical approaches. The statistical regression approach depends on the regression equation established by the atmospheric parameters and the satellite measurements from the spectral channels. This method does not consider the physical characteristics of atmospheric radiation transmission and cannot describe important nonlinearities between geophysical variables and radiances. Therefore, in this method, the accuracy of the retrievals is determined by the temporal and spatial representations of the statistical samples. Even so, this method has advantages due to the efficiency of its calculations. Several scientists have described the eigenvector statistical method. Smith and Woolf illustrated a statistical regression approach to retrieve atmospheric parameters from measured radiance values using eigenvector covariance matrices (Smith and Woolf, 1976). Guan retrieved atmospheric temperature and humidity profiles and surface skin temperature from atmospheric infrared sounder (AIRS) observations with an eigenvector statistical technique based on principal component analysis (Guan, 2006). Jiang implied that temperature and humidity profiles retrieved from AIRS by using eigenvector covariance matrices can meet the basic requirements of atmospheric profile retrieval accuracy: 1 K for temperature and 20% for humidity in 1-km-thick tropospheric layers (Jiang et al., 2006). Use of the eigenvector statistical method for retrieving temperature and humidity profiles from AIRS has also been performed by many other scholars (Zhang et al., 2014; Liu et al., 2008; Smith et al., 2012). Other statistical regression methods, including the ridge regression method (Xi and Wang, 1984), the cumulative sum statistical control method (Zhang and Wang, 1995), the empirical orthogonal function method (Han et al., 2009), and the least-squares method (Xu, 2003), have been widely used to retrieve atmospheric profiles. In recent years, machine learning algorithms have been gradually applied to the field of atmospheric science. Yao demonstrated that the overall root mean square errors of profiles retrieved by the neural networks method are 17% lower over the ocean and 15% lower over land than those obtained by using the statistical retrieval method (Yao and Chen, 2006). Singh retrieved atmospheric temperature and humidity profiles by using neural networks based on the advanced microwave sounding unit (AMSU) over Indian region in real time and reported that the retrieved temperature and humidity profiles showed good agreement with the measurements from the AIRS, with a bias, under 850 hPa, of 3 K and 4 g/kg (Singh and Bhatia, 2006). Paola achieved temperature and water vapor profiles using the random forest technique (MiRTaW) based on observations from the advanced technology microwave sounder (ATMS) (Paola et al., 2018). Malmgren-Hansen presented, for the first time, the use of convolutional neural networks for the retrieval of atmospheric profiles from IASI sounding data and observed a huge benefit to the retrieval accuracy when predicting profiles over clouds (Malmgren-Hansen et al., 2019).

As mentioned above, the statistical approach is dependent on a large training dataset, and the physical nature of atmospheric radiation transmission is not considered, which affects the accuracy of the retrievals. The physical approach aims to retrieve atmospheric temperature and humidity profiles directly from satellite measurements of spectral channel radiation. This approach takes atmospheric radiation transmission into account and does not depend on training samples. Physical methods require prior information of a statistical nature and involve radiative transfer calculations and iterative solutions

(Duncan and Kummerow, 2016). Many methodologies have been proposed to estimate these iterative solutions (Chahine, 1970; Smith, 1970; McMillin, 1991). Among those methodologies, the variational method lays a foundation for retrieving atmospheric parameters from IR hyperspectral and microwave sounder measurements. Li retrieved temperature profiles through Newton nonlinear iteration based on the 1D-Var principle from The International Advanced Television and Infrared Observation Satellite Operational Vertical Sounder (ATOVS) and the accuracy of the retrieval is about 2 K at 1-km vertical solution (Li et al., 2000). Susskind described the basic version of the methodology based on the variational method used by the AIRS Science Team to analyses AIRS data in the presence of clouds and determine atmospheric temperature and humidity profiles (Susskind et al., 2003). Wu reported that the root mean square errors of profiles retrieved from AIRS clear sky measurements over 850 hPa were less than 1 K for temperature profiles and 10% for humidity profiles (Wu et al., 2006). Currently, many investigators have widely used the 1D-Var algorithm to retrieve atmospheric parameters and develop assimilation systems for a variety of microwave sensors, infrared hyperspectral sounders, and ground-based microwave radiometers (Li and Zeng, 1997; Liu and Weng, 2005; Martinet et al., 2017).

A new generation of Chinese geostationary meteorological satellites called Fengyun-4A (FY-4A) was successfully launched into space in 2016. The Geostationary Interferometric Infrared Sounder (GIIRS) onboard FY-4A is the first infrared hyperspectral sounder onboard a geostationary weather satellite with greatly enhanced capabilities for high-impact weather event monitoring, warning, and forecasting. He (He et al., 2019) reported that temperature profiles are available only at altitudes above the cloud top and humidity profiles are not provided in the present operational products released by the Chinese National Satellite Meteorological Center (NSMC). Nearly half of the level 2 operational atmospheric temperature and humidity products from the NSMC are labelled perfect, even in clear sky conditions; under cloudy sky conditions, only 30% of the products are categorized as perfect, according to the quality flag suggested by the Fengyun science team. It is urgent to improve the accuracy and increase the number of the profiles retrieved based on GIIRS observations. Therefore, the 1D-Var physical retrieval algorithm is applied for hyperspectral infrared GIIRS data to retrieve atmospheric temperature and humidity profiles under both clear-sky and partly cloudy conditions in this paper. At the same time, radiosonde data are used to validate the performances of the FY4A operational products from the NSMC and of the profiles retrieved in this study.

2. Data and model

2.1 GIIRS data

The Fengyun-4 (FY-4) series comprises China's second-generation geostationary meteorological satellites. As the first flight unit of the FY-4 series, FY-4A was successfully launched into space on December 11, 2016, carrying the Advanced Geosynchronous Radiation Imager (AGRI), Geostationary Interferometric Infrared Sounder (GIIRS), and the Lightning Mapping Imager (LMI) (Yang et al., 2017). FY-4A's GIIRS is the first high-spectral-resolution advanced IR sounder onboard a geostationary weather satellite, complementing the advanced IR sounders in polar orbit and providing almost continuous temporal, horizontal and vertical observations.

The GIIRS is a Michelson Fourier transform infrared interferometer that measures atmospheric infrared radiation, covering the range of the long-wavelength IR (LWIR) band (700−1130 cm^{-1}) and the mid-wavelength IR (MWIR) band (1650−2250 cm^{-1}) at a spectral resolution of 0.625 cm^{-1}. It has 1650 spectral channels, of which 689 channels are for the LWIR band and 961 channels are for the MWIR band. As FY-4A moves, the GIIRS observes a total of 128 fields of view (FOVs) arranged in a 32 × 4 array, corresponding to an FOV with a 16-km diameter at nadir. The specific GIIRS instrument characteristics are given in Table I (Yu et al., 2020).

In this study, GIIRS level-1 (L1) observed data and level-2 (L2) operational products from December 2019 to January 2020 (winter season) and from July 2020 to August 2020 (summer season) were collected at 0000 to 0100 Coordinated Universal Time (UTC) and 1200 to 1300 UTC. The GIIRS L1 observed data can provide information such as the measured radiation values of the 1650 channels, noise equivalent spectral radiation values and observation points' geographical locations of longitude and latitude. The GIIRS L2 operational products include the temperature profile of the GIIRS, cloud mask, land/sea mask and surface parameters. The GIIRS L1 and L2 datasets can both be downloaded from the Chinese National Satellite Meteorological Center (NSMC).

2.2 Radiosonde data

The radiosonde data of specific synoptic hours from upper-air stations in China are used to estimate the performance of the retrieved profiles and the GIIRS profile products from the NSMC. The radiosonde data are received twice a day, at 0000 and 1200 UTC, from the China Meteorological Data Service Center (CMDC). Sounding observations from December 2019 to January 2020 and from July 2020 to August 2020 from 89 upper-air stations in the China area were used in this paper. The data include observational information such as geopotential height, temperature, dew point temperature, wind direction, wind speed at all specific isobaric levels, and pressure-temperature-humidity layers.

2.3 ERA5 data

In 2018, the European Centre for Medium-Range Weather Forecasts (ECMWF) launched its fifth-generation global climate reanalysis dataset, called ERA5, which is produced using 4D-Var data assimilation in CY41R2 of ECMWF's Integrated Forecast System (IFS), with 137 hybrid sigma/pressure (model) levels in the vertical direction, with the top level at 0.01 hPa. Atmospheric data are available on these levels and are also interpolated to 37 pressure, 16 potential temperature and 1 potential vorticity level(s). The ERA5 dataset has a horizontal resolution of $0.25° \times 0.25°$ (± 31 km at the equator) and a temporal resolution of 1 h (Hersbach et al., 2020). In this paper, atmospheric parameters at 37 pressure levels, including temperature, specific humidity, and ozone mass mixing ratio, were collected at 0000 to 0100 UTC and at 1200 to 1300 UTC as initial guesses for 1D-Var retrieval. Surface level parameters, including surface pressure, geopotential, and skin temperature, were used at the same time. To address the pressure level mismatch, a regression matrix was applied to map the data from the ERA5 37 pressure levels to the 101 levels required by the retrieval, which is consistent with the levels of the U.S. standard profile.

2.4 Forward model

The forward model is one of the most critical components of the retrieval algorithm. It computes radiances in a clear sky corresponding to given atmospheric and surface states as well as Jacobian radiances with respect to atmospheric and surface parameters for use by the retrieval module. In this study, the Community Radiative Transfer Model (CRTM) developed by the United States Joint Center for Satellite Data Assimilation (Weng, 2005) was applied. In the 1D-Var retrieval algorithm, the initial profiles generated from the ERA5 datasets were used as inputs for CRTM. The number of levels in the CRTM model was set to 101, which is consistent with the input profiles for the retrievals.

3. Introduction of retrieval methodology

3.1 Theoretical basis of 1D-VAR retrieval algorithm

The retrieval methodologies adopted for both microwave and infrared radiation are mostly based on finding the solutions by minimizing a cost function of the following form (Rodgers, 1976):

$$\boldsymbol{J}(\boldsymbol{x}) = \left\| \boldsymbol{y} - \boldsymbol{F}(\boldsymbol{x}) \right\|^2 \quad (1)$$

where $\boldsymbol{y}$ and $\boldsymbol{F}(\boldsymbol{x})$ represent the observed radiances and the radiances calculated by the forward model and x is the atmospheric state vector. If both the state vector and the radiances are characterized by Gaussian distributions, then the cost function can be minimized by the following form:

$$\boldsymbol{J}(\boldsymbol{x}) = (\boldsymbol{x} - \boldsymbol{x}_b)^T \boldsymbol{B}^{-1} (\boldsymbol{x} - \boldsymbol{x}_b) + \left[\boldsymbol{y} - \boldsymbol{F}(\boldsymbol{x})\right]^T \boldsymbol{O}^{-1} \left[\boldsymbol{y} - \boldsymbol{F}(\boldsymbol{x})\right] \quad (2)$$

where $\boldsymbol{B}$ and $\boldsymbol{O}$ represent the background error covariance matrix and observation error covariance matrix describing the measurement, respectively; $\boldsymbol{x}_b$ is the background state vector, namely, an a priori vector; $\boldsymbol{F}(\boldsymbol{x})$ is the radiance simulated using the forward model; and $\boldsymbol{y}$ is the observed radiance. The first term of the cost function on the right represents the penalty for departing from the a priori information, while the second term represents the penalty for departing from the measurements. The algorithms used to minimize the cost function include the linear iterative method, the Gauss-Newton nonlinear iterative method, the steepest descent method and the Levenberg-Marquardt method. In this study, the Newton method was adopted to seek the iterative solution to the inversion problem by minimizing this cost function (Martinet, 2015). When the term with $\boldsymbol{y}-\boldsymbol{F}(\boldsymbol{x})$ in the second partial derivative is neglected (Li and Zeng, 1997), the final one-dimensional variational iteration equation can be written as follows:

$$\boldsymbol{x}_{n+1}=\boldsymbol{x}_n+(\boldsymbol{B}^{-1}+\boldsymbol{K}^T\boldsymbol{O}^{-1}\boldsymbol{K})^{-1}\bullet\left[\boldsymbol{B}^{-1}(\boldsymbol{x}_b-\boldsymbol{x}_n)+\boldsymbol{K}^T\boldsymbol{O}^{-1}(\boldsymbol{y}-\boldsymbol{F}(\boldsymbol{x}_n))\right] \quad (3)$$

where n is the iteration number; $\boldsymbol{x}_n$ and $\boldsymbol{x}_{n+1}$ represent the profiles of atmospheric temperature and humidity at steps n and $n+1$ in the iteration process, respectively; and $\boldsymbol{K}$ is the Jacobian matrix containing partial derivatives of $\boldsymbol{y}$ with respect to $\boldsymbol{x}$, calculated by the forward model. The NMC method was utilized to compute the background error covariance matrix from the differences between 48 hours and 24 hours forecasts provided by the ECMWF operational forecasts. The set of forecasts differences consists of two daily runs (starting at 0000 and 1200 UTC) for the period of four months in December 2019 and January, July, and August 2020. To further handle the nonlinearity of the retrieval problem, the DRAD approach is used in the above Newton method to ensure that the retrieval is stable (Lynch et al., 2009). In the DRAD approach, the diagonal element of the observation error covariance matrix $\boldsymbol{O}$ is set to either the difference between the observed and simulated radiances for a particular spectral channel or to the instrument noise plus forward model error:

$$\boldsymbol{O}(j,j) = max\left\{\frac{1}{\alpha}[\boldsymbol{y}_n(j) - \boldsymbol{y}(j)]^2, \boldsymbol{\sigma}^2(j)\right\} \quad (4)$$

where α is the configurable error parameter, which is set to 2 in this paper and $\boldsymbol{\sigma}(j)$ is the instrument noise variance for channel j. The role of α is to limit the magnitude of $\boldsymbol{x}_{n+1} - \boldsymbol{x}_n$ at each iteration step. As the number of iterations increases, the difference term quickly vanishes, and the final solution is obtained. Finally, a chi-square test is used to check the convergence of the retrieval (Divakarla et al., 2014). The chi-square test acts as a gauge of the consistency between the radiances calculated by the forward model and the observed GIIRS radiances relative to instrument noise errors. The equation is as follows:

$$\chi^2 = \sum_{j}^{nchan} \frac{(\boldsymbol{y}_j - \boldsymbol{y}_j^{sim})^2}{\boldsymbol{\sigma}_j} / nchan \quad (5)$$

where $nchan$ is the number of channels used in the retrieval and $\boldsymbol{y}_j^{sim}$ is the simulated radiance using the forward model. The termination criteria of the iteration are an χ^2 less than 0.7 or an iteration number greater than nine.

3.2 GIIRS data matching

To generate the initial guess profiles, it is necessary to collocate the ERA5 datasets with the GIIRS observational field of view by temporal-spatial matching. The first step in the matching process is the spatial interpolation of the ERA5 data on a standard grid to the latitude and longitude of the GIIRS FOV. A bilinear interpolation is performed. The second step is the temporal interpolation of the ERA5 data to the GIIRS observational time. The ERA5 data of the previous hour and the next hour at each GIIRS observation time are used for interpolation. The interpolation in time is conducted using a simple linear method. The final mapping step is the vertical interpolation. The ERA5 profiles are interpolated from their native vertical levels to the 101 levels of the retrievals.

3.3 Treatments of clouds

Clouds have a significant effect on the observed IR radiances. Therefore, accurate treatment of the effects of clouds on the observed GIIRS observations is critical for obtaining accurate atmospheric profiles. In this paper, a cloud-detection method is developed following a cloud clustering algorithm, which is described in detail in the Cross-track Infrared Sounder's (CrIS) environmental data records algorithm (Divakarla et al., 2014). The cloud information is extracted from the 2×2 FOVs, as illustrated in Fig. 1. The FOVs of the GIIRS observation mode are arranged in a 32 × 4 array. Each FOV corresponds to a specific detector and has a spatial horizontal resolution of approximately 16 km. The cloud information is extracted from the four adjacent FOVs (FOV 1, FOV 2, FOV 33, and FOV 34) enclosed in the black circle marked as 1 in Fig. 1. The other four adjacent FOVs within the 32×4 array are subjected to cloud detection in the same way. The cloud mask classification is as follows: clear, partly cloudy or cloudy. Fig. 2 shows an example of the results obtained using the above cloud mask method. Fig. 2 (a) shows the spatial distributions of the GIIRS brightness temperature images of channel 320 (900 cm^{-1}) in the LWIR band in the China area on August 10, 2019, from 1200 to 1340 UTC. The colder the colour is, the more likely the presence of clouds is. The cloud mask classification for each FOV is presented in Fig. 2 (b). A green pixel with a value of 1 means that the FOV is clear; a brown pixel with a value of 2 is partly cloudy FOV; and a blue pixel with a value of 3 is labelled cloudy sky. It is clearly shown that the detected cloudy FOVs (including partly cloudy and cloudy FOVs) in Fig. 2 (b) are consistent with the cold colour areas with lower brightness temperatures in Fig. 2 (a).

After cloud detection, the appropriate retrieval strategy is determined for each FOV depending upon the cloud classification. When the 2×2 FOVs are assigned as clear, the GIIRS radiances within these four FOVs are averaged, and retrieval is performed based on the averaged radiances. When the 2×2 FOVs are classified as cloudy, the 2×2 FOVs are assumed to be covered by enormous clouds, and no retrieval is performed. Instead, the initial guess profiles are reported. For partly cloudy 2×2 FOVs, the measurements are used to estimate the clear part radiances, and retrieval is performed on these clear radiances (Susskind et al., 1998). According to Susskind's cloud-clearing methodology, the cloud-cleared radiances $\overline{\boldsymbol{R}}_{\boldsymbol{i},\boldsymbol{clr}}$ can be written as a linear combination of the measured radiances:

$$\overline{\boldsymbol{R}}_{\boldsymbol{i},\boldsymbol{clr}} = \overline{\boldsymbol{R}}_{\boldsymbol{i},1} + \eta_1(\overline{\boldsymbol{R}}_{\boldsymbol{i},1} - \overline{\boldsymbol{R}}_{\boldsymbol{i},\boldsymbol{k}+1}) + ... + \eta_{\boldsymbol{k}}(\overline{\boldsymbol{R}}_{\boldsymbol{i},1} - \overline{\boldsymbol{R}}_{\boldsymbol{i},2}) \quad (6)$$

where $\overline{\boldsymbol{R}}_{\boldsymbol{i},\boldsymbol{clr}}$ is the simulated clear radiance for channel i within four FOVs; $\overline{\boldsymbol{R}}_{\boldsymbol{i},\boldsymbol{k}+1}$ is the measured radiance, in which at least K+1 FOVs are needed to solve for K cloud formations (K=3 in this paper); and η_k is a channel-independent constant. Once the values of η_k are obtained, the cloud-clear radiances can then be calculated by the above equation.

3.4 Channel selection

While the GIIRS has 1650 channels, it is neither necessary nor optimal to use all the channels in the retrieval process, as the information content of these channels is highly redundant. Therefore, proper selection of GIIRS channels is necessary to lower computing time.

The channel selection method adopted in this study is based on the weighting function (WF) of each channel (Susskind et al., 2003):

$$WF = \frac{\partial(v,\theta,p)}{\partial ln(p)} \quad (7)$$

where $\partial(v,\theta,p)$ represents the transmittance of the channel with a central wavenumber of v, which depends on the absorption coefficient of the absorbed gas in the atmosphere and the vertical distribution of the density; p is the pressure; and θ is the satellite zenith angle. This formula clearly shows that the weighting function represents the contribution of the atmospheric layer centred at the WF peak altitude to the radiance observed by that channel. The channel selection based on the weighting function aims to select the channels with the sharpest weighting functions that are primarily sensitive to the variables being solved for but relatively insensitive to variables not yet solved for. The main contribution of the atmospheric radiation energy to the satellite instrument comes from the pressure layers with the sharpest shapes and largest weighting function values (Liu et al., 2008). To ensure a high vertical resolution, at least one channel is selected for each retrieval level where the peak height of the channel weighting function is located. The channel with the highest peak value and the steepest shape is selected if different channels have the same peak height. For the channels with a peak layer of the weighting function in the lower troposphere, taking near-surface complexity into consideration, two channels are selected in the lower troposphere: the channel with the steepest shape and the channel with the highest peak value. These window channels with peak layers of the weighting function near the surface and with fewer overlapping curves are selected. The

U.S. standard atmospheric profile is used as the CRTM input for channel selection in this paper. The final selected 329 channels are provided in Fig. 3. The black line in Fig. 3 shows the observed brightness temperature spectra of all 1650 GIIRS channels. Superimposed coloured circle symbols indicate the 8 channel subsets forming the final channel selection. The final 329 channels are selected, comprising 15 window channels (magenta), 98 temperature (red), 61 water vapor (blue), 53 ozone (olive), 16 carbon monoxide (purple), 41 carbon dioxide (navy), 18 N_2O (cyan) and 27 HNO_3 (violet) sounding channels.

3.5 Retrieval process framework

The generic framework of the 1D-Var retrieval process for the GIIRS data is illustrated in Fig. 4. The ERA5 datasets collocated with the GIIRS observations by temporal-spatial matching generate the initial guess profiles. Then, a cloud-detection step is carried out to identify the cloud conditions within every FOV. For cloudy FOVs, no retrieval is performed. Instead, the initial guess profiles are reported. For partly cloudy FOVs, the clear part radiance is first simulated by a cloud-clearing method; then, retrieval is performed on the clear part. The CRTM (as the observation operator) and a minimization method for the cost function are included in the retrieval process. Finally, the Newton nonlinear iteration method is adopted in the 1D-Var retrieval to minimize the cost function. If the convergence test cannot be passed, the values of the profiles are updated and put into the CRTM again to run until the final retrieval results are obtained.

4. Results and discussion

The radiosonde data available at the CMDC were used as a reference to validate the quality of the atmospheric profiles retrieved in this study and the FY-4A operational level-2 temperature profiles obtained from the NSMC. To obtain a sufficient sample size to evaluate the retrieval accuracy, four months of radiosonde data in December 2019 and January, July, and August 2020 were selected for validation. The coordinates of each GIIRS FOV are matched with those of each upper air sounding station. Sample pairs that meet the following distance threshold criterion are obtained by setting a threshold of distance on the surface of sphere (Yu et al., 2020):

$$\arccos\left[\sin(lat_G)\sin(lat_S)+\cos(lat_G)\cos(lat_S)\cos(lon_G-lon_S)\right]R\leq 16 \quad (8)$$

where lat_G, lon_G and lat_S, lon_S represent the longitude and latitude of the GIIRS FOV and the sounding station, respectively and R represents the radius of the Earth (6371 km). A distance threshold of 16 km is set according to the spatial resolution of the GIIRS. In addition to spatial matching, the observation times should be taken into consideration. The radiosonde data are received at 0000 and 1200 UTC, twice a day. The retrievals are performed half an hour before and after these times. After spatial and temporal matching, 81 pair stations in China were selected, and the total number of samples for each month was 4860. The parameter describing humidity in the radiosonde data is the temperature of the dew point. To facilitate the comparison of the humidity retrieval results, the temperature of the dew point is converted to the specific humidity, q, following the equations:

$$\ln e=\ln(611.2)+\frac{17.62t_d}{243.12+t_d} \quad (9)$$

$$q = 0.622\frac{e}{p} \quad (10)$$

where e represents vapor pressure; t_d represents the temperature of the dew point; and p is the pressure.

The statistical metrics used to evaluate the accuracy of the inversion profiles include the mean bias (MB) and root mean square error (RMSE), which are defined as follows:

$$MB = \frac{\sum_{i=1}^{N}(x_i - x_i')}{n} \quad (11)$$

$$RMSE = \sqrt{\frac{\sum_{i=1}^{N}(x_i - x_i')^2}{n}} \quad (12)$$

where n represents the number of samples; x_i is the radiosonde value; and x_i' is the retrieval.

4.1 Impact of channel selection

To compare the retrieval accuracy and computational efficiency using the selected 329 channels described in section 3.4 with using all 1650 GIIRS channels, we take every five days in July 2020 as an example. There are 149 radiosonde data under clear conditions and 742 radiosonde data under partly cloudy. The retrieved results using the 329 channels plus all remaining long-wave channels within 700–774.375 cm^{-1} (370 channels) were also analyzed statistically. The MB and RMSE profiles for temperature obtained using 329, 370, and 1650 channels are shown in Fig. (5). In the RMSE sense, the retrievals based on 329 channels have better accuracy compared to those using 370 and 1650 channels from surface to 70 hPa under both clear and partly cloudy conditions, while the MB of all 1650 channels is a little bad. This is probably owing to the high channel correlation and information redundancy of the hyperspectral infrared sounding channels. In the stratosphere, the RMSE and MB of all sets are higher, which may because of radiosonde balloon floating with height increasing. Another reason is that there are few channels whose peak height of WF is located between 50-200 hPa no matter 1650 channels or selected channels. Above 70 hPa, using 1650 channels shows a better performance. This is because that ozone channels (1000–1100 cm^{-1}) whose WF peak altitudes are located near 30 hPa could provide more temperature information in the upper levels; fewer ozone channels are selected in the 329 and 370 channel sets.

The average retrieval time of one FOV is 5.05 seconds using the selected 329 channels and 5.97 seconds of the full channels. The run time for the whole China area is about 2.5 hours of selected channels, saving about 15% time to the 1650 channels.

4.2 Under clear skies

Taking radiosondes as true values, the MB and RMSE profiles of the temperatures retrieved by the 1D-Var approach described in this paper, the level-2 operational products from the NSMC and the ERA5 reanalysis data used as initial guess under clear conditions in December 2019 and January 2020 (winter season) are given in Fig. 6 (a) and Fig. 6 (b), respectively. Fig. 6 (c) and Fig. 6 (d) show the MB and RMSE profiles in July and August 2020 (summer season). The solid lines represent the results retrieved from the 1D-Var approach, the dashed lines represent the ERA5 reanalysis data, and the dash-dot lines represent the NSMC level-2 operational products. Due to the lack of radiosonde data above 100 hPa in the winter season, the results are shown only from 1000 hPa to 100 hPa in Fig. 6 (a) and Fig. 6 (b), while the errors from 1000 hPa to 10 hPa are presented in Fig. 6 (c) and Fig. 6 (d). The number of sample sizes used to calculate the MBs and RMSEs at each pressure level is given on the right vertical coordinate. The first column number represents both the retrieved results and the ERA5 data, and the second column number represents the L2 operational products. The number of sample sizes at each level decreases as the altitude decreases because radiosonde data near the surface are more absent than those at high levels. It can be obviously seen that there is a large negative deviation up to 2 K for the NSMC L2 operational products below 800 hPa in both winter and summer. The most accurate temperature retrievals for the 1D-Var approach and L2 operational products are both between 800 hPa and 200 hPa, with MBs between ∓ 0.5 K. The MBs of the results retrieved from the 1D-Var approach are less than those of the L2 operational products above 200 hPa. The RMSEs of the 1D-Var-retrieved temperatures are less than those of the L2 operational products for the whole atmosphere, especially in summer. The RMSEs of the temperatures retrieved from the 1D-Var approach are approximately 1 K in summer, except near the ground. In the winter season, the RMSEs of the 1D-Var-retrieved temperatures are slightly higher, from 1.5 K to 2 K. Compared with the ERA5 reanalysis data, the retrieved results are improved between 800 hPa and 300 hPa both in winter and summer seasons. The RMSEs of the temperatures retrieved from the 1D-Var approach decrease about 0.1 K compared with the ERA5 data from 800 hPa to 300 hPa, but the MBs of the retrievals are larger in the whole atmosphere. Above 200 hPa, the RMSEs of the retrieved temperatures increase by more than 2 K. This is the same case that appears in the L2 products. This may have resulted due to the following three reasons: there are few temperature sounding channels whose WF peak values are located near or above the upper troposphere; errors are caused by sounding balloons floating at high altitudes; and the number of samples above the upper troposphere is reduced with limited radiosonde data. Fig. 7 shows scatter plots of the temperatures received with the radiosondes. Fig. 7 (a) and Fig. 7 (c) indicate that the correlation coefficient between the 1D-Var retrievals and the radiosonde data is 0.992 in winter and 0.993 in summer, which indicates high correlation. The average RMSE of the whole troposphere in winter is 2.045 K, and the MB is 0.126 K, while in summer, the average RMSE of the whole atmosphere is 1.388 K and the MB is 0.23 K. The retrieved values and radiosonde values are evenly distributed on both sides of the line $y = x$. The scatter plots of the NSMC level-2 products in Fig. 7 (b) and Fig. 7 (d) show slightly higher RMSEs, with 2.243 K in winter and 2.302 K in summer.

Because humidity profiles are not provided in the L2 operational products from the NSMC, only the performance of the retrieved humidity profiles and ERA5 reanalysis data was evaluated through comparison to the radiosonde data. The distributions of the RMSE and MB profiles of the retrieved humidity in the troposphere are shown in Fig. 8. The solid line in Fig. 8 represents the RMSE, while the dashed line represents the MB. As shown in Fig. 8, the highest RMSE (approximately 2.5 g/kg) occurs near the surface at 925 hPa in both winter and summer. Except for the near-surface level, the RMSE of each level in the troposphere is less than 2 g/kg and decreases with height. Meanwhile, the dash-dot line and the dotted line stand for the RMSE and MB of the ERA5 humidity in Fig. 8, respectively. The retrieved humidity appears to agree better with the radiosonde data than the ERA5 data between 800 hPa and 300 hPa both in winter and summer seasons. Scatterplots of the retrieved humidity data and the radiosonde data are given in Fig. 9. The results show that the correlation coefficient is 0.926 in winter and 0.948 in summer. The retrieved values and radiosonde values show good correlation. In winter, the mean RMSE of the humidity in the troposphere is 0.748 g/kg, and the MB is -0.027 g/kg; in summer, the mean RMSE is 1.040 g/kg, and the MB is 0.217 g/kg. The retrieval accuracy of humidity in winter is slightly better than that in summer. There is a consistent underestimation in summer in Fig. 9 (b), which is consistent with the fact that water vapor content that is too high or too low in the atmosphere is not conducive to improving the retrieval accuracy (Zong, 2020).

4.3 Under partly cloudy conditions

One of the characteristics of the NSMC L2 operational products is that the temperature values are missing at altitudes below the cloud top and humidity profiles are not provided at the present when the FOV is assigned as cloudy according to the L2 cloud mask products. An example of a single-profile temperature (a) and humidity (b) retrieval from the L2 operational products compared with a radiosonde profile (station number 54511) under partly cloudy conditions on August 1, 2020 at 0000 UTC is presented in Fig. 10. The dashed line in Fig. 10 represents the profile retrieved by the 1D-Var approach, the dotted dashed line represents the L2 operational product, and the solid line represents the radiosonde observations. The L2 temperature profile below 300 hPa has no value, and the 1D-Var-retrieved temperature profile is closer to the radiosonde profile in both the troposphere and stratosphere than is the L2 profile (Fig. 10 a). The humidity comparison is illustrated in Fig. 10 (b). The retrieved humidity profile is still very close to the radiosonde profile. Fig. 10 (c) presents the performance of minimization of the cost function for this single-profile retrieval. The χ^2 values versus iteration number for this single-profile were recorded. The red line represents the iteration criteria 0.7. It can be clearly seen that its value decreases with the increase of iterations the criterion is met after the seventh iteration.

Fig. 11 (a) and Fig. 11 (b) show the MBs and RMSEs, respectively, of the 1D-Var-retrieved temperature profiles, the ERA reanalysis data and the L2 products from the NSMC compared with radiosonde data under partly cloudy conditions in December 2019 and January 2020 (winter season). Fig. 11 (c) and Fig. 11 (d) show the MBs and RMSEs, respectively, in July and August 2020 (summer season). The number of samples at each pressure level is given on the right side of Fig. 11 (b) and Fig. 11 (d). The first column number represents both the retrieved results and the ERA5 data, and the second column number represents the sample size of the L2 operational products. It can be clearly seen that the sample size of the L2 operational products decreases sharply with decreasing height because of the limited data below the cloud top, especially in Fig. 11 (d). The level 2 temperature profile is available only at altitudes above the cloud top under partly cloudy conditions. In contrast, the 1D-Var-retrieved temperatures can be produced at the whole atmospheric vertical level under partly cloudy conditions. Whether in winter or summer, the RMSEs of the temperature profiles at all vertical levels retrieved from 1D-Var are far less than those of the level 2 products. Compared with Fig. 6 and Fig. 11, it can be clearly seen that the temperature retrieval accuracy under partly cloudy conditions is similar to that under clear conditions. The most accurate retrievals occur between 800 hPa and 300 hPa, and the RMSE value was reported to be approximately 1 K. Comparison of the retrievals and the radiosonde data show smaller RMSE values between 800 hPa and 300 hPa than the comparison of the ERA5 reanalysis data and radiosonde data. Above 200 hPa, the higher the altitude is, the larger the deviation between retrievals and ERA5 is. The inversion accuracy in winter is slightly worse than that in summer.

Scatterplots of the retrieved temperature and level-2 products under partly cloudy conditions are shown in Fig. 12. The statistical correlation coefficient, MB and RMSE of the 1D-Var method are all smaller than those of the Level 2 product. This again shows that the 1D-Var inversion accuracy is higher than that of the operational method. The correlation coefficient between the retrievals and the radiosonde data is 0.966 in winter and 0.991 in summer. In winter, the average temperature RMSE is 2.371 K, and the MB is 0.384 K; in summer, the average RMSE is 1.404 K and the MB is 0.310 K. Under partly cloudy conditions, the retrieved temperatures are generally higher than the target temperatures, similarly to the results obtained under clear sky conditions.

Fig. 13 shows the RMSE and MB profiles of the humidity profile obtained from 1D-Var and ERA5 reanalysis data under partly cloudy conditions in the troposphere. This are no humidity profiles obtained from the NSMC products. The solid line represents the RMSE, while the dashed line represents the MB of retrieved humidity. The dash-dot line and the dotted line stand for the RMSE and MB of the ERA5 humidity, respectively. As shown in Fig. 13, the highest RMSE (approximately 3 g/kg) occurs near the surface in both winter and summer, and the deviation tends to decrease with increasing height. The RMSEs of the retrieved humidity are also smaller than the ERA5 humidity between 800 hPa and 300 hPa. Scatterplots of the retrieved humidity with the radiosonde data are given in Fig. 14. The correlation coefficient is 0.892 in winter and 0.953 in summer. The mean winter RMSE of the humidity profile is 0.917 g/kg, and the RMSE value is 1.567 g/kg in summer.

In addition, it should be noted that possible error sources in the retrieval process that are accounted for the retrieval uncertainties: few temperature sounding channels whose WF peak values are located near the higher troposphere as mentioned above account for the inaccuracy in the high levels; the cloud detection is not accurate, and the clear-sky FOVs and partly-cloudy FOVs could not be completely detected; in temporal matching, the inputs for the forward model adopted the initial profiles at 0000 and at 1200 UTC and the corresponding GIIRS data had a deviation of 0 to 1 hour; in spatial matching, the satellite FOVs and the spatial grid point of the ERA5 reanalysis data are not completely spatially matched.

5. Conclusions

As the first infrared hyperspectral sounder onboard a geostationary weather satellite, FY-4A's GIIRS can provide 3-dimensional atmospheric temperature and humidity fields with high scanning frequencies and spatial resolutions. Therefore, the improvement of retrieval precisions based on hyperspectral infrared data, especially on stationary satellite platforms, has great significance. The 1D-Var physical retrieval algorithm is used in this paper to simultaneously retrieve the temperature and humidity profiles under both clear-sky and partly cloudy conditions. Collocated radiosonde observations from upper-air stations in the China area are used to validate the data quality of the retrieved temperature and humidity profiles along with the NSMC level-2 operational products during the periods from December 2019 to January 2020 and from July 2020 to August 2020. The results are as follows:

1) The RMSE accuracy of the 1D-Var temperature retrievals is within 2 K in the whole troposphere except for near the surface under clear sky conditions. The most accurate

temperature retrievals are between 800 hPa and 200 hPa with RMSEs less than 1 K. The correlation coefficients between the 1D-Var retrievals and radiosonde data are all approximately 0.99, and the retrieved temperature profile is closer to the radiosonde data than are the level-2 products in both winter and summer.

2) The temperature values in the NSMC level-2 operational products are missing at altitudes below the cloud top; temperature and humidity profiles can be produced at each vertical level by 1D-Var method under partly cloudy skies.

3) The retrieval accuracy under partly cloudy conditions can maintain the same performance as that under clear conditions. The temperature RMSE profiles at all vertical levels from 1D-Var are far less than those of the level-2 products. The mean RMSE in the troposphere is within 2 K.

4) Only the performance of the retrieved humidity profiles was evaluated in comparison to the radiosonde data since humidity profiles are not provided in the NSMC L2 operational products. The average RMSE of the retrieved humidity profiles is within 2 g/kg, whether under clear or cloudy skies.

5) The temperature and humidity retrievals have improved performance compared to the ERA5 reanalysis data between 800 hPa and 300 hPa both in winter and summer seasons whether under clear or cloudy sky conditions. Furthermore, the retrievals can provide the atmospheric profiles with a higher temporal resolution than the ERA5 reanalysis data.

Overall, temperature and humidity profiles can be provided by the 1D-Var physical retrieval algorithm with high precisions under all weather conditions based on hyperspectral infrared observations uploaded on the geostationary satellite platform.

Acknowledgments. The authors would like to thank the editor and reviewers for their helpful comments on the manuscript. This work was supported in part by the National Key Research and Development Program of China under Grant 2018YFC1507302, in part by the National Natural Science Foundation of China under Grant 41975028.

REFERENCES

Chahine, M. T., 1970: Inverse problems in radiative transfer: Determination of atmospheric parameters. *J. Atmos. Sci.*, **27**(6), 960–967.

Divakarla, Murty., and Coauthors, 2014: The CrIMSS EDR Algorithm: Characterization, Optimization, and Validation. *J. Geophys. Res. Atmos*., **119**(8), 4953-4977.

Duncan, D. I., and C. D. Kummerow, 2016: A 1DVAR retrieval applied to GMI: Algorithm description, validation, and sensitivities. *J. Geophys. Res. Atmos*., **121**(12), 7415–7429.

Guan, L., 2006: Retrieving Atmospheric Profiles from MODIS/AIRS Observations. I. Eigenvector Regression Algorithms. *J. Nanjing Inst. Meteorol*., **6**, 756–761.

Han, J., L. Guan, Z. H. Wang, and X. H. Zhang, 2009: The Influence of Surface Temperature on the Retrieval of Clear-Sky Air Temperature Vertical Profile. *Atmospheric science research and application*., **1**, 80–86.

He, M., D. H. Wang, W. Y. Ding, Y. J. Wan, Y. H. Chen, and Y. Zhang, 2019: A Validation of Fengyun4A Temperature and Humidity Profile Products by Radiosonde Observations. *Remote Sens*., **11**(17), 2038-2057.

Hersbach, H., and Coauthors, 2020: The ERA5 global reanalysis. *Q. J. Roy. Meteor. Soc*., **146**(730), 1999-2049.

Jiang, D. M., C. H. Dong, and L. W. Song, 2006: Preliminary Study on the Capacity of High Spectral Resolution Infrared Atmospheric Sounding Instrument using AIRS Measurements. *Journal of Remote Sensing*., **4**, 586–592.

Kaplan, L. D., 1959: Inference of atmospheric structure from remote radiation measurements. *J. Opt. Soc. Amer*., **49**, 1004–1007.

King, J. I. F., 1956: The radiative heat transfer of planet Earth. Scientific Uses of Earth Satellites. University of Michigan Press, 133–136.

Li, J., and Q. C. Zeng, 1997: Atmospheric infrared remote sensing and its retrieval problems in clear sky: I. Theoretical study. *Chin. J. Atmos. Sci*., **21**, 1–9.

Li, J., and Q. C. Zeng, 1997: Atmospheric infrared remote sensing and its retrieval problems in clear sky: II. Research on retrieval test. *Chin. J. Atmos. Sci*., **21**, 87–95.

Li, J., W. W. Wolf, W. P. Menzel, W. Zhang, H. L. Huang, and T. H. Achtor, 2000: Global soundings of the atmosphere from ATOVS measurements: The algorithm and validation. *J. Appl. Meteor*., **39**(8)**,** 1248–1268.

Liu, H., C. H. Dong, W. J. Zhang, and P. Zhang, 2008: Retrieval of clear air atmospheric temperature profiles using AIRS observations. *Acta Meteorol. Sinica*. **66**(4), 513–519.

Liu, Q. H., and F. Z. Weng, 2005: One-dimensional variational retrieval algorithm of temperature, water vapor, and cloud water profiles from advanced microwave sounding unit (AMSU). *IEEE Trans. Geosci. Remote Sens*., **43**(5), 1087–1095.

Lynch, R., J. L. Moncet, and X. Liu, 2009: Efficient nonlinear inversion for atmospheric sounding and other applications. *Appl. Opt*., **48**(10), 1790-1796.

Malmgren-Hansen, D.; V. Laparra, A. A. Nielsen, and G. Camps-Valls, 2019: Statistical retrieval of atmospheric profiles with deep convolutional neural networks. *ISPRS. J. Photogramm.*, **58**, 231–240.

Martinet, P., A. Dabas, J. M.Donier, T. Doffer, O. Garrouste, R. Guillot, 2015:1D-Var temperature retrievals from microwave radiometer and convective scale model. *Tellus A.*, **67**, 27925.

Martinet, P., D. Cimini; F. D. Angelis, G. Canut, V. Unger, R. Guillot, D. Tzanos, and A. Paci, 2017: Combining ground-based microwave radiometer and the AROME convective scale model through 1DVAR retrievals in complex terrain: An Alpine valley case study. *Atmos. Meas. Technol.*, **10**(9), 3385-3405.

McMillin, L. M., 1991: Evaluation of a classification method for retrieving atmospheric temperatures from satellite measurements. *J. Appl. Meteor.*, **30**(4), 432–446.

Menzel, W. P., T. J. Schmit, P. Zhang, and J. Li, 2018: Satellite-based atmospheric infrared sounder development and applications. *Bull. Amer. Meteorol. Soc.*, **99**(3), 583–603.

Paola, F. D., and Coauthors, 2018: MiRTaW: An Algorithm for Atmospheric Temperature and Water Vapor Profile Estimation from ATMS Measurements Using a Random Forests Technique. *Remote Sensing.*, **10**(9), 1398–1425.

Pougatchev, N., T. August, X. Calbet, T. Hultberg, O. Oduleye, P. Schluessel, B. Stiller, K. St Germain, and G. Bingham, 2009: IASI temperature and water vapor retrievals – error assessment and validation. *Atmos Chem Phys.*, **9**(17), 6453-6458.

Rodgers, C. D., 1976: Retrieval of atmospheric temperature and composition from remote measurements of thermal radiation. *Rev. Geophys.*, **14**(4), 609–624.

Singh, D., and R. C. Bhatia, 2006: Study of temperature and moisture profiles retrieved from microwave and hyperspectral infrared sounder data over Indian regions. *Indian Radio Space Phys*., **35**(4), 286–292.

Smith, W. L., 1970: Iterative solution of the radiative transfer equation for the temperature and absorbing gas profile of an atmosphere. *Appl. Opt.*, **9**(9), 1993–1999.

Smith, W. L., and Coauthors, 2012: Dual-Regression Retrieval Algorithm for Real-Time Processing of Satellite Ultraspectral Radiances. *J. Appl. Meteorol. Clim*., **51**(8), 1455–1476.

Smith, W. L., and H. M. Woolf, 1976: The Use of Eigenvectors of Statistical Covariance Matrices for Interpreting Satellite Sounding Radiometer Observations. *J. Atmos. Sci*., **33**(7), 1127–1140.

Strow, L. L., S. E. Hannon, S. De Souza-Machado, H. E. Motteler, and D. Tobin, 2003: An overview of the AIRS radiative transfer model. *IEEE Trans. Geosci. Remote Sens*., **41**(2), 303-313.

Susskind, J., C. D. Barnet, and J. Blaisdell, 1998: Determination of atmospheric and surface parameters from simulated AIRS/AMSU/HSB sounding data: Retrieval and cloud clearing methodology. *Adv. Space Res.*, **21**(3), 369–384.

Susskind, J., C. D. Barnet, and J. Blaisdell, 2003: Retrieval of atmospheric and surface parameters from AIRS/AMSU/HSB data in the presence of clouds. *IEEE Trans. Geosci. Remote Sens*., **41**(2), 390–409.

Weng, F., Y. Han, P. van Delst, Q. Liu, T. Kleespices, B. Yan, and L. Marshal. 2005： JCSDA Community 38 Radiative Transfer Model. 14th Int. TOVS study Conf., Beijing, China, Int. TOVS Working Group, 217-222.

Wu, X. B., J. Li, W. J. Zhang, F. Wang,2005: Atmospheric Profile Retrieval with AIRS

Data and Validation at the ARM CART Site. *Adv. Atmos. Sci*., **22**(5), 647–654.

Xi, R., and J. S. Wang, 1984: Modern practical regression analysis. Guangxi: Guangxi People's Publishing House.

Xu, G. M., 2003: Inversion: theory and Application. Beijing: Seismological Press.

Yang, J., Z. Q. Zhang, C. Y. Wei, F. Lu, and Q. Guo, 2017: Introducing the new generation of Chinese geostationary weather satellites, Fengyun-4. *Bull. Amer. Meteorol. Soc*., **98**(8), 1637–1658.

Yao, Z. G., and H. B. Chen, 2006: Retrieval of Atmospheric Temperature Profiles with neural network inversion of microwave radiometer data in in 6 Channels near 118.75 GHz. *Scientia Meteor Sinica.*, **26**(3), 3252–3259.

Yu, P. P., C. X. Shi, L. Yang, and S. Shan, 2020: A new temperature channel selection method based on singular spectrum analysis for retrieving atmospheric temperature profiles from FY-4A/GIIRS. *Adv. Atmos. Sci*., **37**(7), 735–750

Zhang, J., Z. L. Li, J. Li, and J. L. Li, 2014: Ensemble Retrieval of Atmospheric Temperature Profiles from AIRS. *Adv. Atmos. Sci*., **31**(3), 559–569.

Zhang, P. C., and Z. H. Wang, 1995: Fundamentals of atmospheric microwave remote sensing. Beijing: China Meteorological Press.

Zong, M. X., 2020: Estimating the Inversion Accuracy of Atmospheric Temperature and Water Vapor Profile under Limb Sounding. *J ApplMeteor Sci*., **31**(4), 471–481.

Table 1. Specification for GIIRS onboard FY-4A

Parameter	Performance
Spectral bandwidth	Long wave: 700−1130 cm^{-1} Mid wave: 1650−2250 cm^{-1}
Spectral channels	Long wave: 689 Mid wave: 961
Spectral resolution	Long wave: 0.625 cm^{-1} Mid wave: 0.625 cm^{-1}
Sensitivity	Long wave: 0.5–1.1 $mW/m^{-2} \cdot sr \cdot cm^2$ Mid wave: 0.1–0.14 $mW/m^{-2} \cdot sr \cdot cm^2$
Operational model	China area: 5000×5000 km^2 Mesoscale area: 2000×2000 km^2
Spatial resolution	16 km
Temporal resolution	China area: 67 min Mesoscale area: 35 min
Calibration accuracy	1.5 K (3σ) radiation 10 ppm (3σ) spectrum

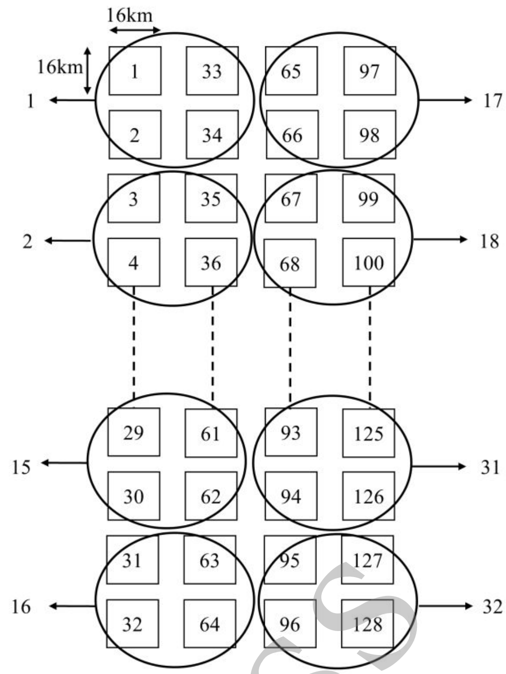

Fig. 1. The distribution of 128 GIIRS FOVs and 32 cloud mask products. (box: GIIRS FOV; circle: cloud mask product)

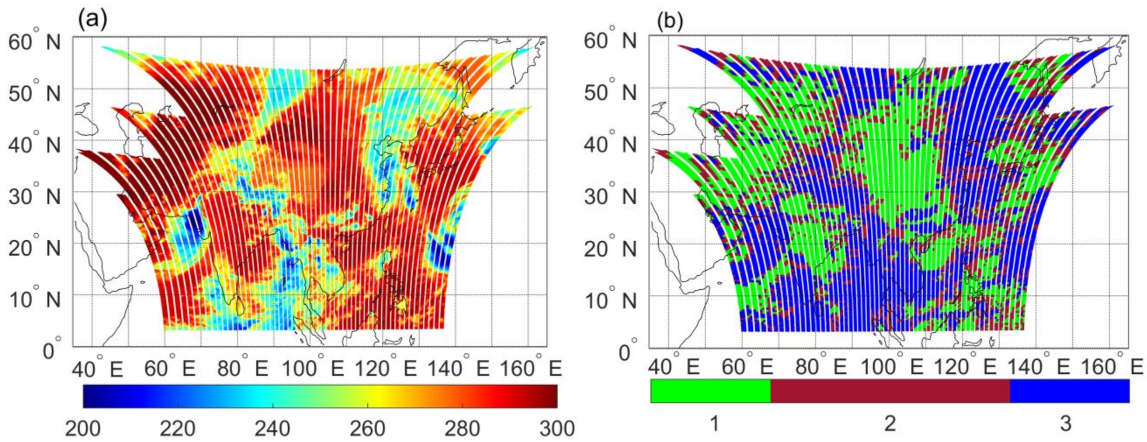

Fig. 2. The GIIRS-observed brightness temperatures of channel 320 (900 cm^{-1}) (a) and the cloud detection results (b) in the China area on August 10, 2019 from 1200 to 1340 UTC.

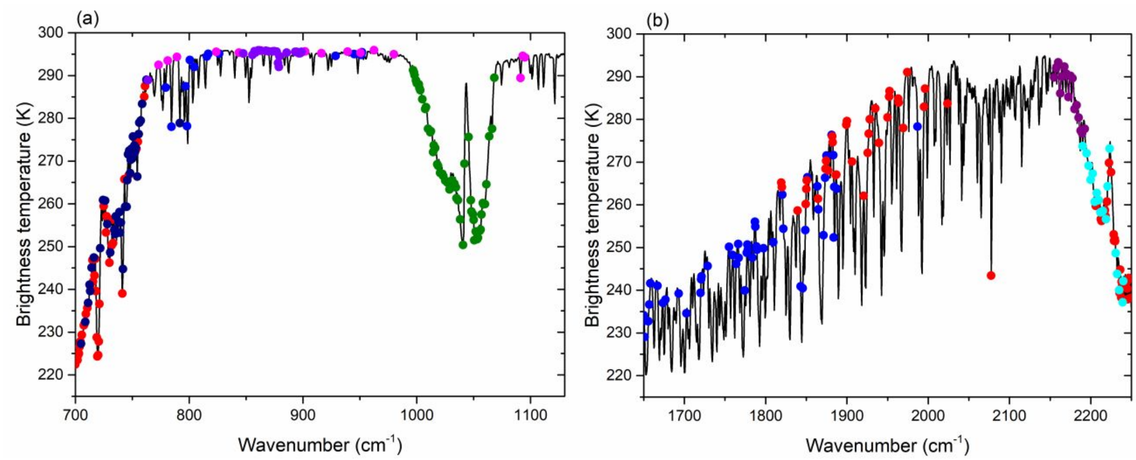

Fig. 3. Selected retrieval channels at the GIIRS's LWIR band (a) and MWIR band (b).

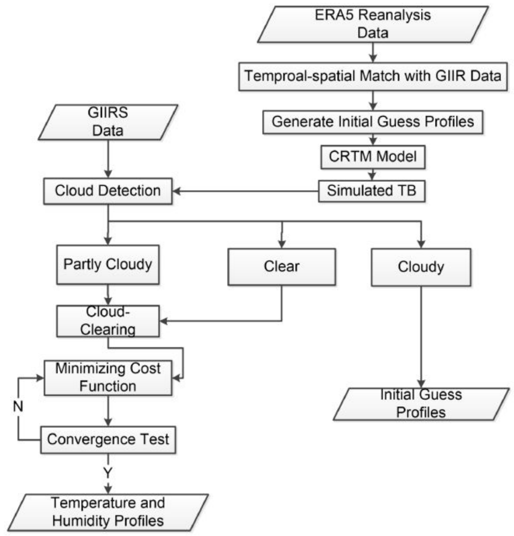

700

701 **Fig. 4.** Flow chart of the 1D-Var retrieval process for the GIIRS.

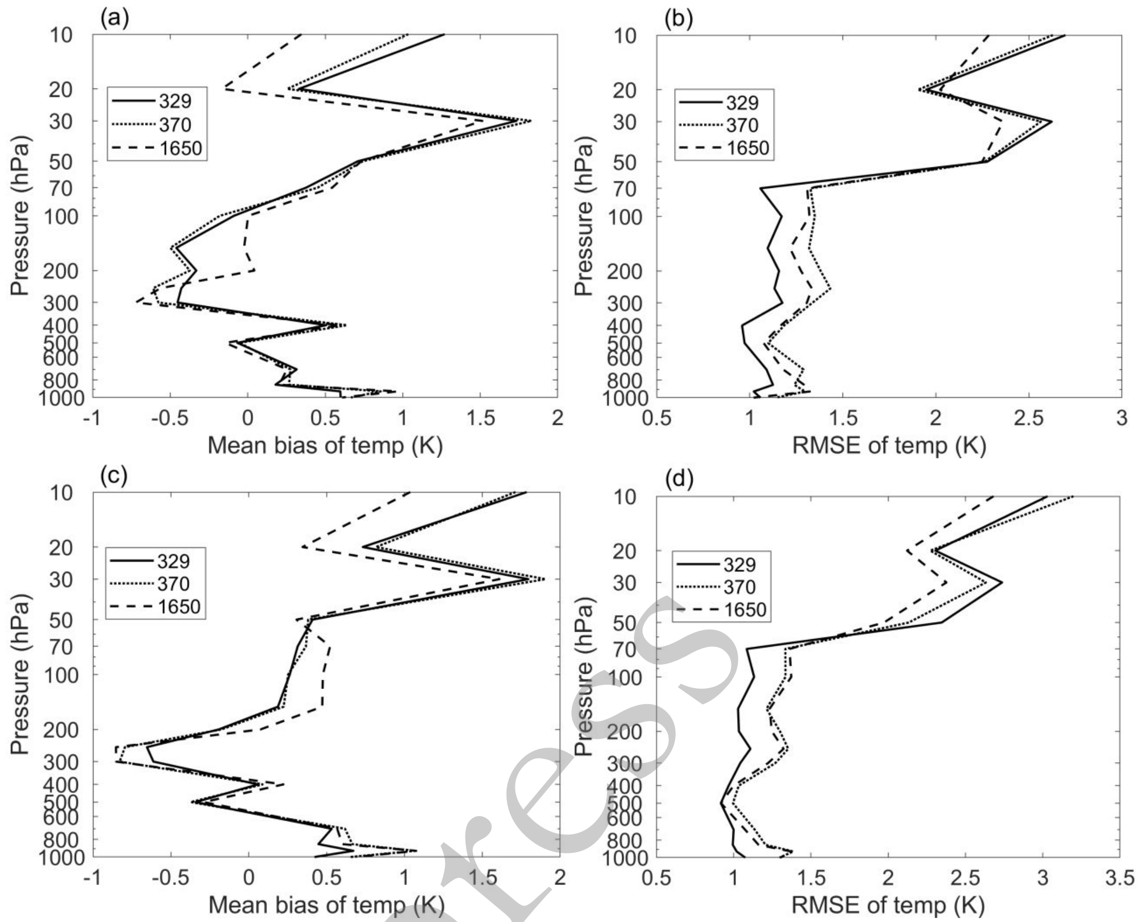

Fig. 5. The MB (a) and RMSE (b) profiles of the retrieved temperature under clear condition and the MB (c) and RMSE (d) profiles under partly cloudy condition in July 2020.

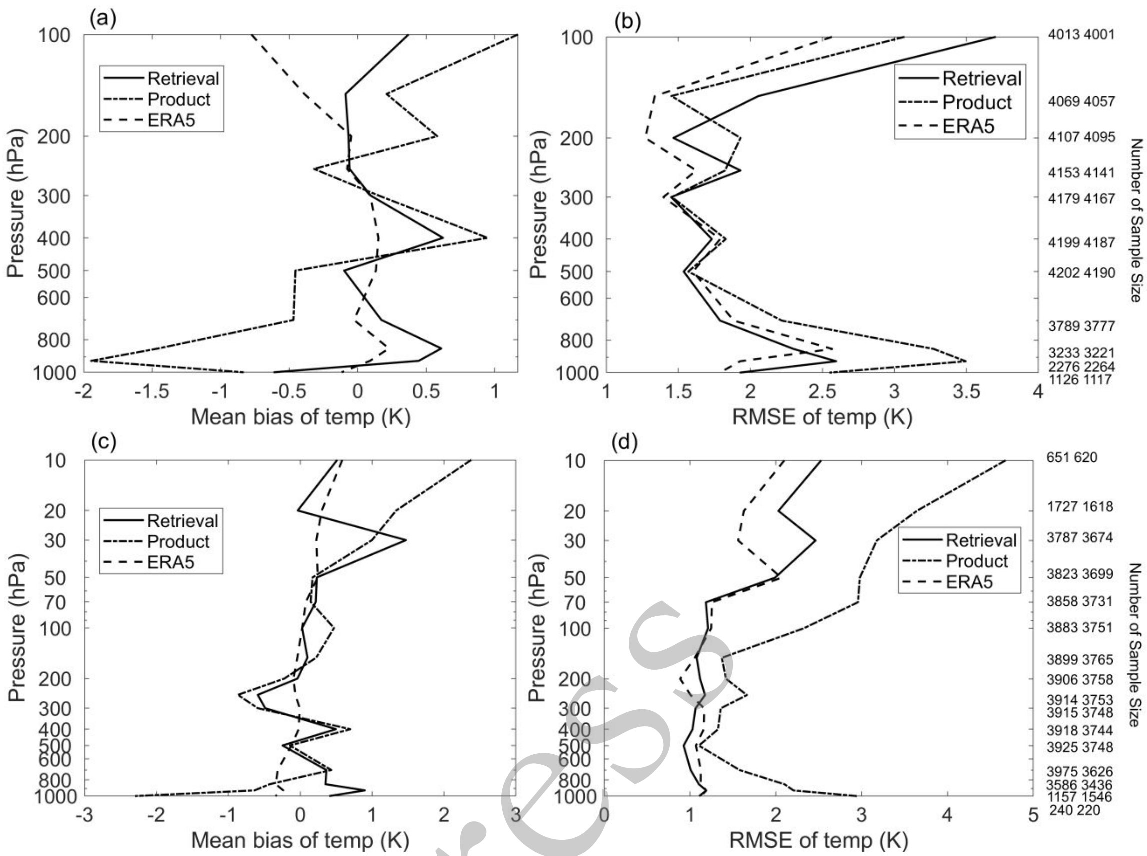

Fig. 6. The MB (a) and RMSE (b) profiles of the inversion temperatures under clear conditions in December 2019 and January 2020 and the MB (c) and RMSE (d) profiles of the inversion temperatures under clear conditions in July and August 2020. The solid lines represent the results retrieved from the 1D-Var approach, the dashed lines represent the ERA5 reanalysis data, and the dash-dot lines represent the NSMC L2 operational products.

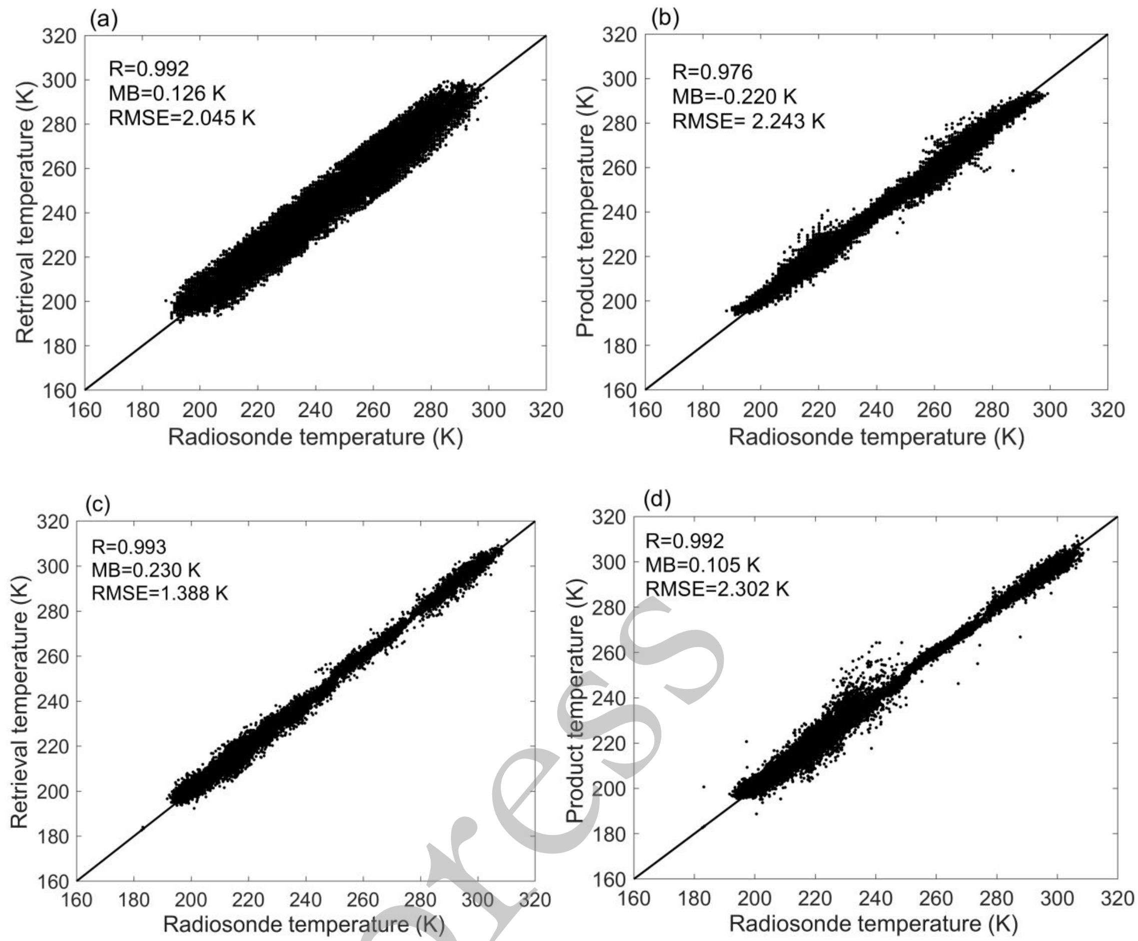

Fig. 7. Scatterplots of retrieved (a) and level-2 product (b) temperatures with radiosonde observations for the whole atmosphere under clear-sky conditions in December 2019 and January 2020, and the same plots for retrieved (c) and level-2 product (d) temperatures in July and August 2020.

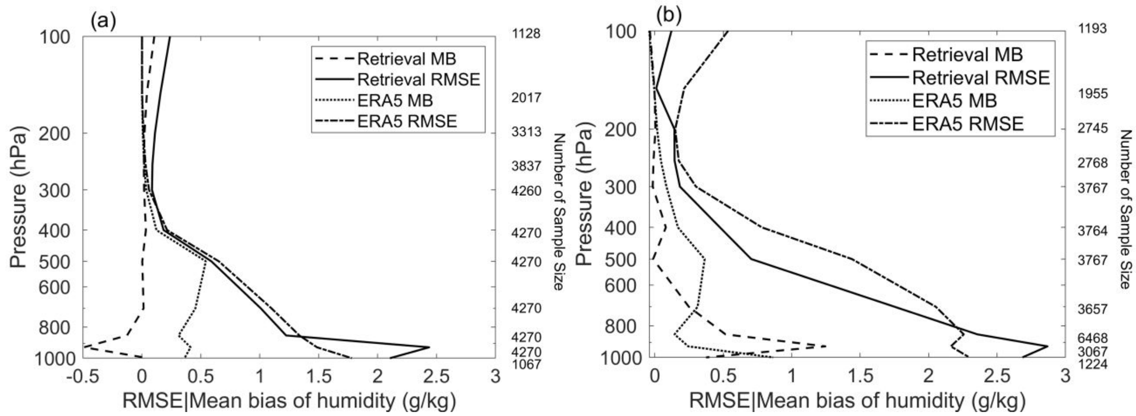

Fig. 8. Errors of the humidity profiles under clear conditions in December 2019 and January 2020 (a) and in July and August 2020 (b).

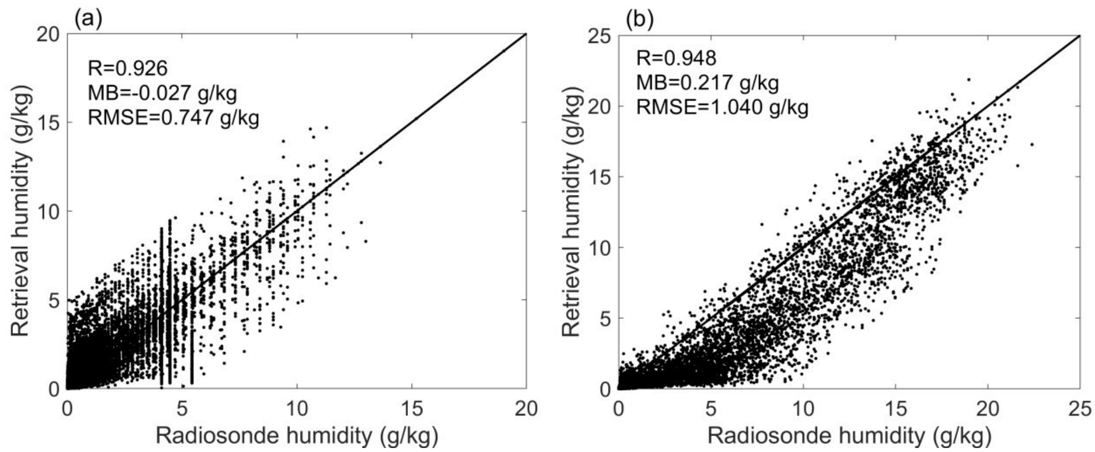

Fig. 9. Scatterplots of the humidity profiles in the troposphere under clear conditions in December 2019 and January 2020 (a) and in July and August 2020 (b).

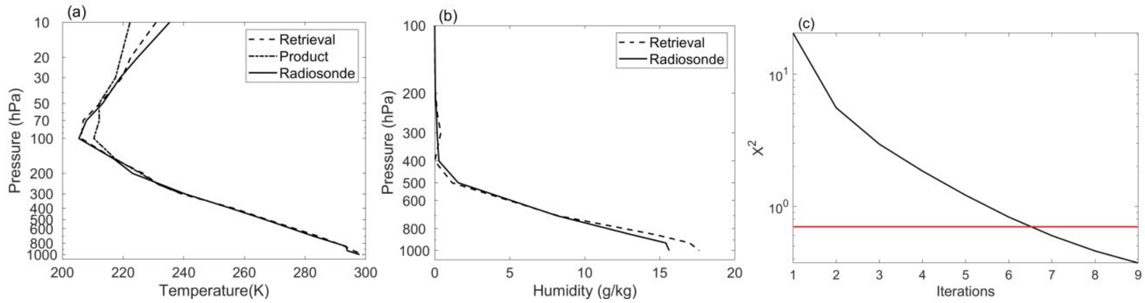

Fig. 10. An example of temperature (a) and humidity (b) retrievals compared with radiosonde data under partly cloudy conditions and χ^2 values versus iteration number (c) on August 1, 2020 at 0000 UTC.

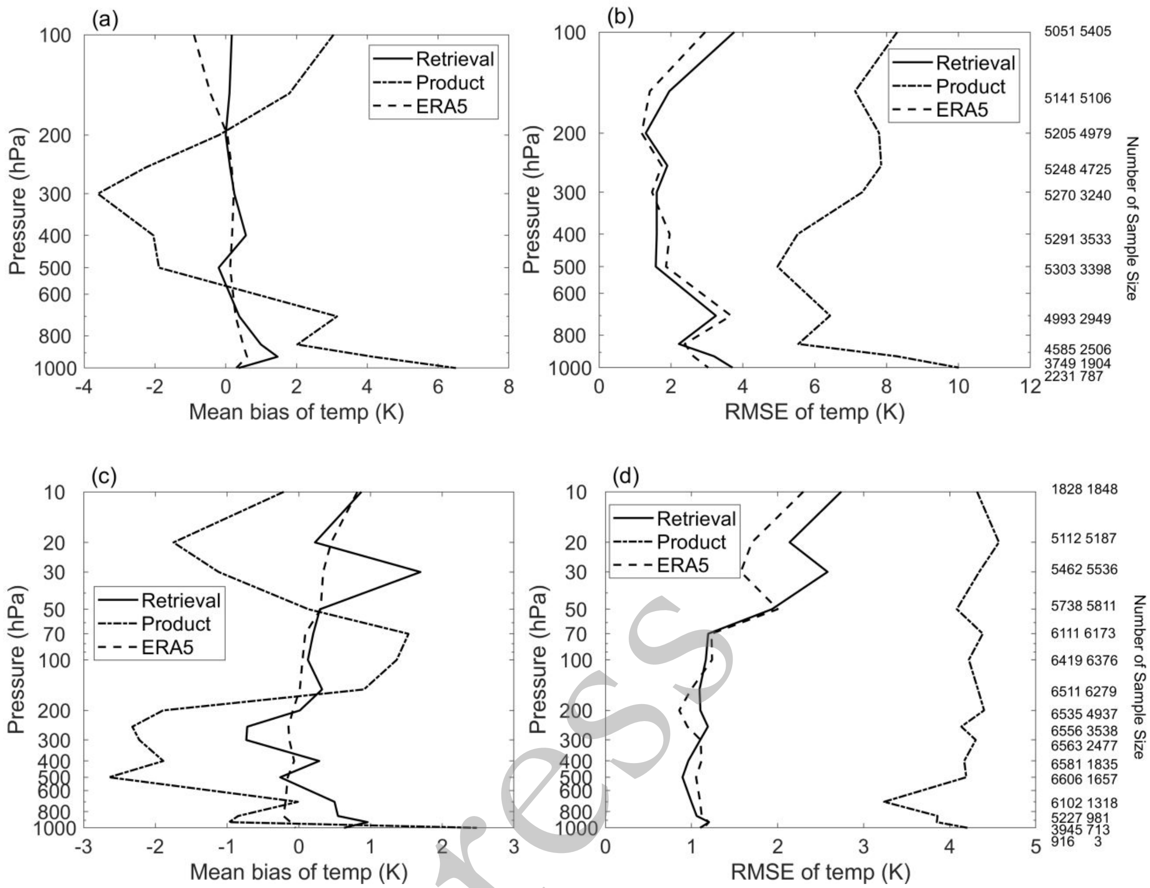

Fig. 11. The MB (a) and RMSE (b) profiles of the inversion temperatures under partly cloudy conditions in December 2019 and January 2020 and the MB (c) and RMSE (d) profiles of the inversion temperatures under partly cloudy conditions in July and August 2020. The solid lines represent the results retrieved from the 1D-Var approach, the dashed lines represent the ERA5 reanalysis data, and the dash-dot lines represent the NSMC L2 operational products.

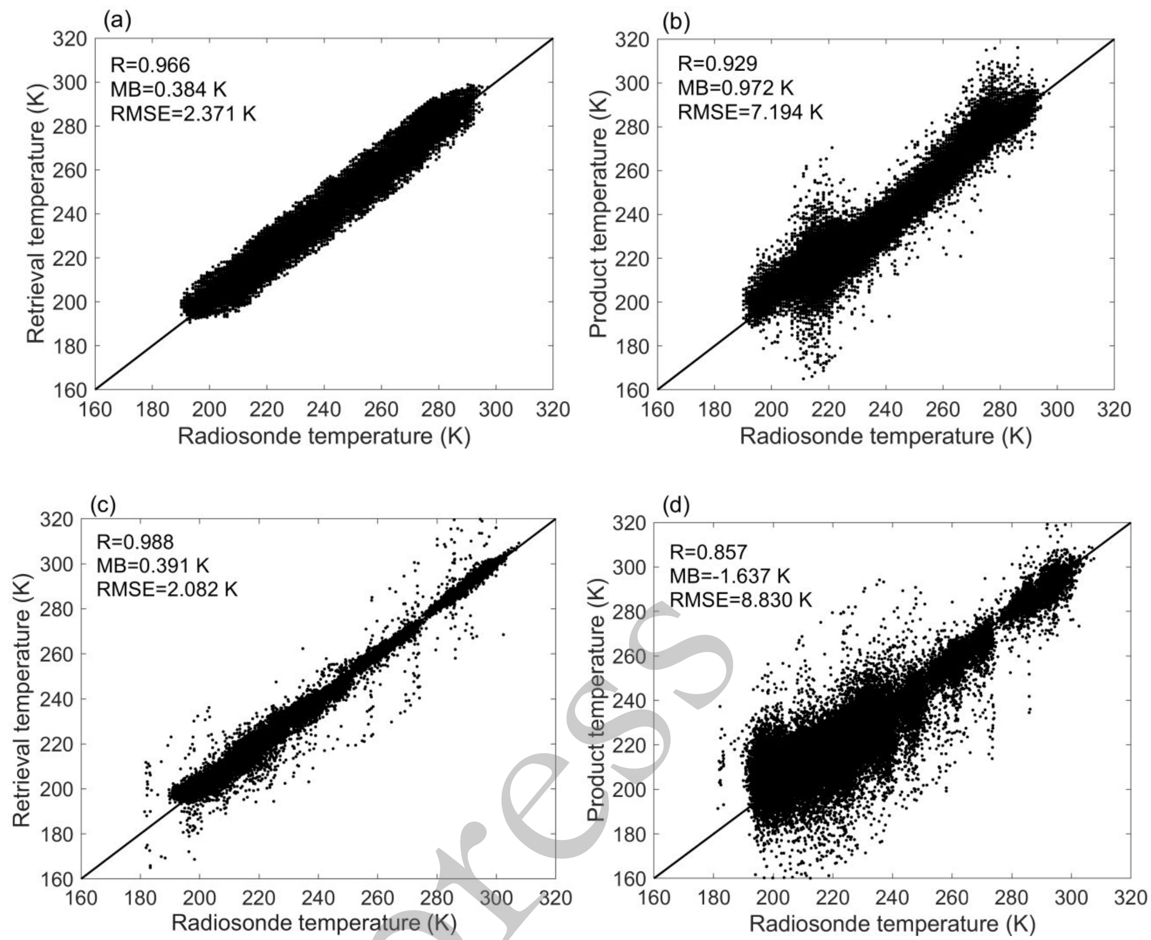

Fig. 12. Scatterplots of retrieved (a) and level-2 product (b) temperatures with radiosonde observations for the whole atmosphere under partly cloudy conditions in December 2019 and January 2020 and the same plots of retrieved (c) and level-2 product (d) temperatures in July and August 2020.

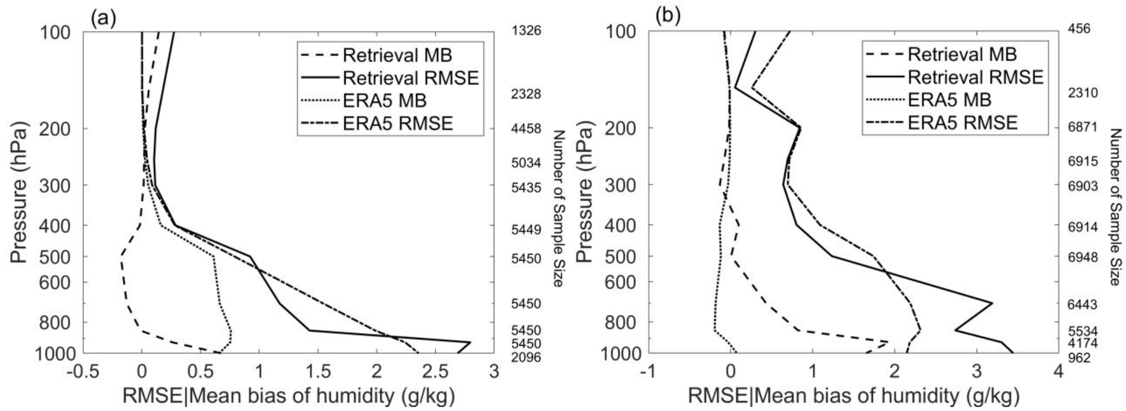

Fig. 13. The humidity error profiles under partly cloudy conditions in December 2019 and January 2020 (a) and in July and August 2020 (b).

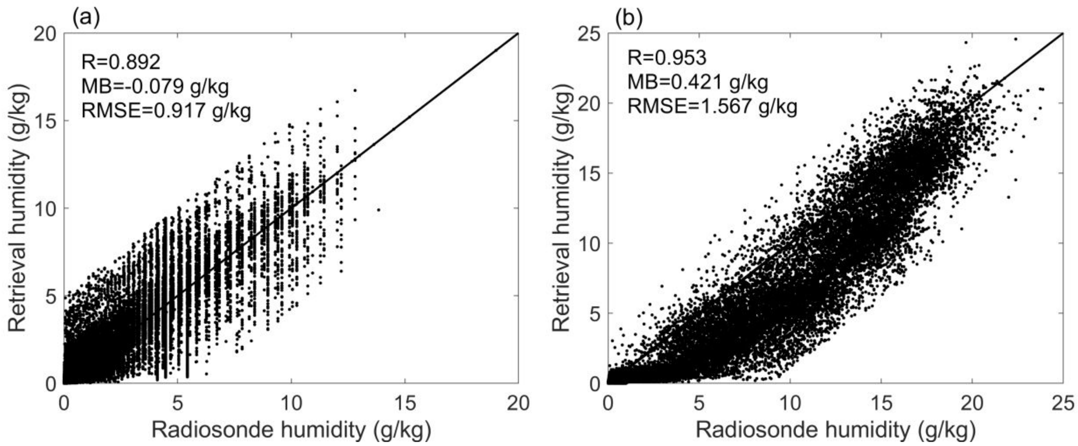

Fig. 14. Scatterplots of the humidity profiles in the troposphere under partly cloudy conditions in December 2019 and January 2020 (a) and in July and August 2020 (b).